Chinese Journal of Chemical Engineering 89 (2026) 13–24

Contents lists available at ScienceDirect

Chinese Journal of Chemical Engineering

journal homepage: www.elsevier.com/locate/CJChE

Full Length Article

Design and optimization of a high-efficiency distillation process for cellulosic fuel ethanol integrated with thermal coupling and molecular sieve adsorption

Xuefeng Feng [1, 2], Shuaishuai Lu [1, 2], Xuan Du [1, 2], Shaolan Zhuang [1, 2], Zhongqi Ren [1, 2], Zhongwei Ding [1, 2], Qunsheng Li [1, 2, *], Weiying Feng [3, *], Hongkang Zhao [1, 2, *]

[1] *Engineering Research Center of Preparation Technology of Ultra-Pure Chemicals for Integrated Circuits, Ministry of Education, Beijing University of Chemical Technology, Beijing 100029, China*
[2] *State Key Laboratory of Chemical Resource Engineering, Beijing University of Chemical Technology, Beijing 100029, China*
[3] *School of Materials Science and Engineering, Beihang University, Beijing 100191, China*

ARTICLE INFO

Article history:
Received 26 June 2025
Received in revised form
3 August 2025
Accepted 6 August 2025
Available online 1 September 2025

Keywords:
Cellulosic fuel ethanol
Three-columns distillation process
Distillation–molecular sieve coupling
Aspen Plus simulation
Total annual cost (TAC)
Carbon dioxide emission cost

ABSTRACT

To address the challenges of high energy consumption and prominent costs in the traditional three-columns distillation process for cellulosic fuel ethanol, a distillation–molecular sieve coupling separation process is proposed. This process integrates a three-column (crude distillation column, first distillation column, second distillation column) system with a 3A molecular sieve adsorption deep dehydration unit. A thermal coupling network is constructed *via* differential pressure design (steam from medium/high-pressure columns as mutual heat sources, reboiler liquid waste heat for feed preheating), and molecular sieve adsorption conditions are optimized. The study first performs a thermodynamic consistency test on the ethanol–water system, determines optimal non-random two-liquid (NRTL) model binary interaction parameters *via* experimental data regression for Aspen Plus simulation. Aiming at minimum total annual cost (TAC), Aspen Plus is used to optimize process parameters (theoretical tray number, feed location, reflux ratio, side-draw position, *etc.*). Economic analysis shows this process reduces CO_2 emission costs by 27.56%, TAC by 15.58% (to 5.123×10^6 USD·a^{-1}), and increases ethanol purity to >99.6%, providing an effective solution for green, efficient separation.

1. Introduction

Against the backdrop of the global energy structure's accelerated transition towards low-carbon forms, cellulosic fuel ethanol, as a typical second-generation biofuel, has emerged as a vital strategic option for alleviating fossil energy crises and reducing carbon emissions in the transportation sector. It benefits from extensive raw material sources (such as lignocellulosic biomass including straw and wood chips), non-competition with arable land, and high carbon cycle efficiency [1,2]. After undergoing processes like pretreatment, enzymatic saccharification, and fermentation of lignocellulosic materials, the resulting cellulosic fuel ethanol fermentation broth contains complex components, such as water, methanol, higher alcohols, aldehydes, organic acids, and undegraded sugars. High-efficiency separation technologies are indispensable for enhancing ethanol purity [3–5]. Nevertheless, this separation process confronts significant technical challenges. Firstly, ethanol and water form an azeotropic system (azeotropic point at 78.15 °C, with an ethanol volume fraction of 95.57%), making it arduous to produce anhydrous ethanol directly *via* conventional distillation. Secondly, impurities in the fermentation broth interfere with the mass transfer efficiency during separation and the performance of adsorbents, rendering traditional single separation techniques inadequate to meet industrial requirements in terms of energy consumption, cost, and product stability [6–9].

Traditional separation technologies exhibit pronounced limitations in the purification of cellulosic fuel ethanol. Conventional

* Corresponding authors.
E-mail addresses: buctlqs@126.com (Q. Li), fengweiying@buaa.edu.cn (W. Feng), 2022500026@buct.edu.cn (H. Zhao).

https://doi.org/10.1016/j.cjche.2025.08.005

distillation, constrained by azeotropic equilibrium, can only elevate ethanol concentration to the azeotropic composition, failing to achieve deep dehydration. Although azeotropic distillation was once applied, it has been phased out due to environmental pollution caused by toxic entrainers like benzene [10–12]. The currently widely adopted extractive distillation technology, using low-toxic solvents such as ethylene glycol, still suffers from high reboiler energy consumption (1.8–2.2 $MJ \cdot kg^{-1}$ ethanol) because of the solvent's high boiling point (197.3 °C) and large circulation volume. Moreover, the high-viscosity solvent tends to cause tray blockages, significantly increasing equipment maintenance costs. The molecular sieve adsorption method, leveraging the preferential water adsorption properties of 3A zeolite molecular sieves (water adsorption capacity 15% to 20% (mass), ethanol adsorption <1% (mass)), achieves dehydration through pressure-swing adsorption (PSA) or temperature-swing adsorption (TSA), cutting energy use by 30% to 40% relative to extractive distillation [13–15]. However, when treating low-concentration cellulosic ethanol fermentation broth (water content >85%), the dynamic adsorption capacity of molecular sieves drops sharply (≈12% more adsorbent is required for every 1% decrease in ethanol concentration) and the regeneration cycle lengthens exponentially with increasing water content, leading to steep rises in both capital and operating expenditures. In addition, organic acids and aldehydes in the broth undergo reversible or irreversible adsorption on the active sites of molecular sieves, shortening their service life and diminishing dehydration efficiency, thereby limiting the stand-alone adsorption route [15,16].

While these individual technologies have been intensively studied, their inherent drawbacks have spurred researchers to explore hybrid schemes that can synergistically compensate for their respective weaknesses. Against this backdrop, distillation–molecular sieve coupling separation processes have emerged as a promising next-generation solution. The core innovation of this coupling lies in its ability to (i) exploit the high throughput and established infrastructure of distillation for bulk concentration and (ii) employ molecular sieves only for the final deep-dehydration step, where their intrinsic selectivity is most valuable [16,17]. Compared with conventional stand-alone processes, the coupled scheme exhibits three unique advantages: (1) Energy efficiency—by concentrating the ethanol stream to 85% to 90% (mass) prior to adsorption, the adsorbent inventory and regeneration duty are reduced by >60%, translating into an overall energy saving of 50% to 55% over extractive distillation; (2) capital cost reduction—smaller sieve columns and lower solvent circulation translate to 20% to 30% lower installed cost; (3) environmental footprint—complete elimination of volatile entrainers avoids benzene emissions and simplifies wastewater treatment [17,18]. The key scientific breakthrough enabling this synergy is the precise matching of operating windows: distillation is terminated just before the molecular sieve's dynamic capacity collapses, while the subsequent PSA/TSA step is optimized to handle the residual water load without excessive regeneration energy. This effectively resolves the "low-concentration penalty" that plagues stand-alone molecular sieves and mitigates the "azeotropic barrier" that limits distillation alone [19].

Building on this concept, Huang *et al.* [20] proposed an integrated distillation–membrane separation process for a 100 $t \cdot h^{-1}$ ethanol–water mixture, projecting >50% energy savings over conventional distillation, although its extension to ethanol–water–acetic acid systems remain under development. Sharma and Wankat [21] designed temperature-swing-adsorption–distillation and pressure-swing-adsorption–distillation hybrids for the isopropanol–water azeotrope, achieving 99.9999% (mol) isopropanol from a 10% (mol) feed; the PSA–distillation variant showed the largest energy reduction. Ritter *et al.* [22] systematically summarized four coupling topologies (overhead, side-stream, or bottom-stream feeding to PSA; PSA product recycle to the column; feed pre-treatment by PSA; side-stream PSA polishing), providing a design map for different purity and throughput targets. Wang *et al.* [23] employed a precision gravimetric apparatus to obtain room-temperature water/ethanol vapor adsorption isotherms on 3A zeolite and starch-based biosorbents. At $P/P_0 = 0.6$, potato starch exhibited a water-to-ethanol sorption ratio of 64.2, outperforming cellulose and 3A zeolite; the Langmuir model best described the 3A system (average relative deviation <5%), supplying reliable parameters for process simulation. Chaibi *et al.* [24] used dynamic TGA to quantify single-component adsorption kinetics of water and ethanol on 3A, 4A and 5A LTA zeolites (20–45 °C). 3A showed the highest water uptake, initial rate, and diffusion coefficient, while apparent ethanol uptake was attributed to trace water co-adsorption, defining an optimal temperature window for maximum selectivity. Kinetic modelling indicated that a pseudo-first-order model accurately captured the data, from which activation energies were derived. Gabrus *et al.* [25] investigated TSA regeneration of 3A and 4A zeolites, identifying 130 °C as the minimum temperature for effective water desorption within the β-cages; structural collapse occurred near 800 °C, setting the upper thermal stability limit for these adsorbents.

This study focuses on the distillation section in fuel ethanol production for process design and optimization. Aiming at the technical bottleneck of excessive energy consumption in the traditional three-columns distillation process (crude distillation column, first distillation column, second distillation column), a distillation-3A molecular sieve coupling process is innovatively proposed to provide an efficient technical solution for the industrial separation and purification of fuel ethanol. Through full-process modeling and process parameter optimization using the Aspen Plus simulation platform, the economic efficiency and environmental friendliness of the production process are systematically improved, providing theoretical support and engineering practice references for technological upgrading in the renewable energy field.

2. Thermodynamic Modeling of Complex Systems and Construction of Multidimensional Economic Evaluation System

2.1. Thermodynamic consistency test of ethanol–water system

During the experimental determination of complete vapor–liquid equilibrium (VLE) data including temperature (T), pressure (P), liquid composition (x), and vapor composition (y), the obtained experimental data may contain errors due to environmental interference, measurement equipment precision limitations, and human reading errors. Direct application of unvalidated data in simulation calculations will seriously affect the accuracy of simulation results, leading to significant deviations from actual operating conditions.

Therefore, to ensure the reliability of experimental data, rigorous evaluation of their accuracy is necessary before applying VLE data to research or engineering practices. Thermodynamic consistency testing is an effective method to judge the credibility of experimental data. Specifically, all experimentally measured VLE data should be subjected to consistency testing based on the Gibbs–Duhem (G–D) equation. The G–D equation holds a pivotal position in thermodynamic theory, precisely describing the

inherent relationship between activity coefficients or fugacity coefficients of solution components under constant temperature and pressure conditions. Its mathematical expression is shown in Eq. (1):

$$\sum x_i \mathrm{d}\,(\ln \gamma_i) = -\sum x_i \frac{H_i^{\mathrm{E}}}{RT^2}\mathrm{d}T + \sum x_i \frac{V_i^{\mathrm{E}}}{RT}\mathrm{d}P \tag{1}$$

where H_i^{E} is the excess enthalpy of component i; V_i^{E} is the excess volume of component i; x_i is the liquid-phase mole fraction of component i; γ_i is the activity coefficient of component i.

In 1951, Herington proposed the integral test method [26]. Given that the measurement of VLE data is typically conducted under isothermal or isobaric conditions, the validation of experimental data can be classified into two scenarios: isothermal and isobaric. For binary systems, the G–D equation in Eq. (1) can be transformed into Eq. (2):

$$x_1 \mathrm{d}\,(\ln \gamma_1) + x_2 \mathrm{d}\,(\ln \gamma_2) = -\frac{H^{\mathrm{E}}}{RT^2}\mathrm{d}T + \frac{V^{\mathrm{E}}}{RT}\mathrm{d}P \tag{2}$$

Under isothermal conditions, the G–D equation obtained by simplifying Eq. (2) is expressed as Eq. (3):

$$x_1 \mathrm{d}(\ln \gamma_1) + x_2 \mathrm{d}(\ln \gamma_2) = \frac{V^{\mathrm{E}}}{RT}\mathrm{d}P \tag{3}$$

Under typical conditions, the right-hand side of the equation equals zero. Therefore, Eq. (3) can be further simplified to Eq. (4):

$$x_1 \mathrm{d}(\ln \gamma_1) + x_2 \mathrm{d}(\ln \gamma_2) = 0 \tag{4}$$

Under isobaric conditions, the simplified G-D equation derived from Eq. (2) is presented as Eq. (5):

$$x_1 \mathrm{d}\ln \gamma_1 + x_2 \mathrm{d}\ln \gamma_2 = -\frac{H^{\mathrm{E}}}{RT^2}\mathrm{d}T \tag{5}$$

Under isobaric conditions, the excess enthalpy (H^{E}) varies with the composition of the system. Since the experimentally measured VLE data are typically obtained under constant pressure conditions, this variable must be considered. Given the difficulty in directly obtaining H^{E}, the Herington integral method was employed to perform a definite integral calculation of the above equation within the range of x_1 from 0 to 1. The specific expression is as follows:

$$\int_{x_1=0}^{x_1=1} \ln\frac{\gamma_2}{\gamma_1}\mathrm{d}x_1 = \int_{x_1=0}^{x_1=1} \frac{H^{\mathrm{E}}}{RT^2}\mathrm{d}T \tag{6}$$

The Herington semi-empirical method was employed to simplify both sides of Eq. (6). For the left-hand side of Eq. (6), a curve was plotted to establish an error evaluation model, and the allowable error D was introduced as the evaluation criterion. Its calculation formula is shown in Eq. (7), where S_{A} and S_{B} represent the areas between the curve and the x-axis above and below the x-axis, respectively.

$$D = \left|\frac{(S_{\mathrm{A}} - S_{\mathrm{B}})}{(S_{\mathrm{A}} + S_{\mathrm{B}})}\right| \times 100 \tag{7}$$

The right-hand side of Eq. (6) is represented by the parameter J, and its calculation formula is shown in Eq. (8).

$$J = 150 \times \frac{T_{\max} - T_{\min}}{T_{\min}} \tag{8}$$

When $|D-J|<10$, the experimental data are determined to pass the thermodynamic consistency test. Conversely, if $|D-J|\geq 10$, the experimental data are considered to have failed the test, indicated unreliability and required rejection.

In the distillation process of fuel ethanol, the core objective is to achieve efficient separation of ethanol and water. Based on the above analysis and derivation, the integral test method was adopted to conduct thermodynamic consistency testing for the ethanol–water system. The VLE data of ethanol–water measured at 101.3 kPa are listed in Table 1, and subsequent research will be carried out for in-depth analysis based on these data.

The vapor–liquid equilibrium relationship can be expressed as:

$$Py_i = \gamma_i x_i P_i^{\mathrm{s}} \tag{9}$$

where P is the normal pressure (101.3 kPa), and P_i^{s} is the saturation vapor pressure of component i at the experimental temperature. The value can be calculated by the Antoine equation, and its expression is shown in Eq. (10).

$$\ln P^{\mathrm{s}} = A - \frac{B}{T + C} \tag{10}$$

The Antoine constants A, B, and C for ethanol and water were obtained *via* Aspen Plus. When used in conjunction with Eq. (10), the pressure unit is mmHg (1 mmHg = 0.133 kPa) and the temperature unit is K. The specific values of A, B, and C are listed in Table 2.

Based on the Antoine constants and experimental data in Table 1, the saturation vapor pressures P_i^{s} and activity coefficients γ_i at different temperature points were calculated, followed by the solution of $\ln(\gamma_1/\gamma_2)$. The calculation results are listed in Table 3.

Based on the calculation results in Table 3, a relationship curve of $\ln(\gamma_1/\gamma_2)$ *versus* x_1 was plotted (see Fig. 1). The integral area calculation function in Origin was used to obtain the areas S_{A} and S_{B} above and below the x-axis, which were substituted into Eq. (11) to calculate the error. Meanwhile, the value of J was calculated, and the analysis was carried out according to the judgment criteria of the test method.

$$D = \left|\frac{(0.286332 - 0.265853)}{(0.286332 + 0.265851)}\right| \times 100 = 3.708638 \tag{11}$$

Table 1
Vapor–liquid equilibrium data of ethanol–water at 101.3 kPa.

P/kPa	T/°C	x_1	x_2	y_1	y_2
101.3	100	0	1	0	1
	96.15	0.015	0.985	0.138	0.862
	92.45	0.035	0.965	0.262	0.738
	86.65	0.100	0.900	0.435	0.565
	83.52	0.182	0.818	0.524	0.476
	81.71	0.291	0.709	0.585	0.415
	80.70	0.392	0.608	0.609	0.391
	79.92	0.502	0.498	0.648	0.352
	79.55	0.542	0.458	0.667	0.333
	78.85	0.632	0.368	0.712	0.288
	78.50	0.748	0.252	0.782	0.218
	78.48	0.794	0.206	0.811	0.189
	78.25	0.845	0.155	0.854	0.146
	78.18	0.898	0.102	0.899	0.101
	78.23	0.948	0.052	0.945	0.055
	78.30	1	0	1	0

Note: x_1 is the liquid-phase mole fraction of ethanol, and x_2 is the liquid-phase mole fraction of water; y_1 is the vapor-phase mole fraction of ethanol, and y_2 is the vapor-phase mole fraction of water.

Table 2
Antoine constants *A*, *B*, *C* for ethanol and water.

Component	*A*	*B*	*C*	*T*/K
Ethanol	18.91	3803.98	−41.68	–
Water	18.30	3816.44	−46.13	351.45–373.15

Table 3
Calculation results of saturation vapor pressures and activity coefficients.

T/°C	P_1^s/kPa	P_2^s/kPa	γ_1	γ_2	$\ln(\gamma_1/\gamma_2)$
100	223.11	101.19	–	1.0013	–
96.15	194.76	87.95	4.8213	1.0069	1.5659
92.45	170.82	76.84	4.4236	1.0100	1.4772
86.65	137.77	61.55	3.2062	1.0318	1.1342
83.52	122.33	54.43	2.3760	1.0820	0.7869
81.71	114.25	50.73	1.7769	1.1708	0.4171
80.70	109.92	48.76	1.4295	1.3342	0.0691
79.92	106.40	47.12	1.2316	1.5164	−0.2076
79.55	105.03	46.53	1.1889	1.5774	−0.2831
78.85	102.24	45.59	1.0487	1.9845	−0.6378
78.50	100.71	44.57	1.0491	1.9845	−0.6376
78.48	100.62	44.52	1.0327	2.0564	−0.6890
78.25	99.67	44.07	1.0252	2.1942	−0.7609
78.18	99.36	43.91	1.0182	2.3293	−0.8271
78.23	99.51	44.05	1.0148	2.4383	−0.8765
78.30	99.86	44.15	1.0147	–	–

Note: P_1^s is the saturation vapor pressure of ethanol, and P_2^s is the saturation vapor pressure of water; γ_1 is the activity coefficient of ethanol, and γ_2 is the activity coefficient of water.

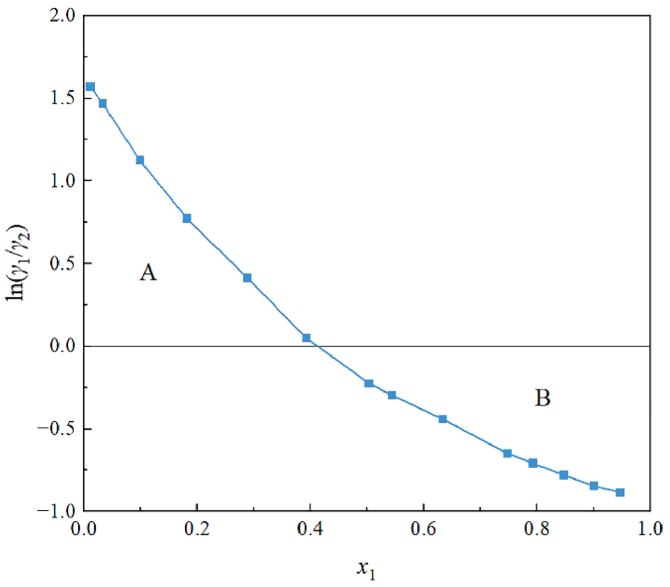

Fig. 1. Integral test results for ethanol–water system.

$$J = 150 \times \frac{T_{max} - T_{min}}{T_{min}} = 150 \times \frac{373.15 - 351.33}{351.33} = 9.32 \quad (12)$$

$$|D - J| = 5.61 < 10 \quad (13)$$

According to the criteria of the integral test method, the set of experimental data was determined to have successfully passed the thermodynamic consistency test. This result indicates that the measured VLE data of ethanol–water exhibit good reliability, which can be used as valid evidence for subsequent fitting regression analysis to obtain binary interaction parameters, providing solid data support for related research.

2.2. Selection of parameter regression method and thermodynamic model

The ethanol–water system belongs to a typical non-ideal polar system, with the operating pressure maintained within 1 MPa. Under these conditions, NRTL, Wilson, and UNIQUAC models are suitable thermodynamic models for this system [27]. However, when simulating with the pre-set binary interaction parameters of ethanol–water in Aspen Plus, significant deviations were found between the simulation results and existing literature data, indicating that relying solely on existing parameters is insufficient to ensure simulation accuracy. Thus, experimental VLE data were employed to perform fitting regression analysis on binary interaction parameters, aiming to obtain more reliable parameter values for input into Aspen Plus and support subsequent simulation calculations.

The VLE data of ethanol–water listed in Table 1 have passed the thermodynamic consistency test, confirming their high reliability. Based on this, the study further utilized these data for binary parameter fitting regression to improve the accuracy of simulation calculations. Specifically, Aspen Plus software was first used to fit the experimental data with three conventional thermodynamic models (NRTL, Wilson, and UNIQUAC), yielding the corresponding binary interaction parameters for each model (Table 4). These parameters were then input into Aspen Plus for simulation to obtain the calculation results of the three models. Finally, a detailed comparative analysis was conducted between the calculation results and experimental data (Tables 5–7), where $T(\text{exp})$ and $T(\text{cal})$ represent the experimental and calculated values of temperature (unit: °C), $x_1(\text{exp})$ and $x_1(\text{cal})$ denote the experimental and calculated values of ethanol liquid-phase mole fraction, and $y_1(\text{exp})$ and $y_1(\text{cal})$ represent the experimental and calculated values of ethanol vapor-phase mole fraction. Through this systematic analysis process, the fitting effects of each model parameter and their impacts on simulation results can be accurately evaluated, providing a scientific basis for the rational selection of thermodynamic models.

Through in-depth analysis of the data presented in Tables 5–7, it is evident that the three thermodynamic models (NRTL, Wilson, and UNIQUAC) all exhibit certain deviations between calculated and experimental values when simulating the ethanol–water system. To screen the optimal thermodynamic simulation method for this system, a systematic comparison was conducted from two key dimensions: maximum deviation and average deviation, with results detailed in Table 8. Close inspection of Table 8 reveals that in terms of the core accuracy indicator average deviation, the NRTL model stands out with significantly lower values, demonstrating better fitting performance and simulation accuracy than the other two models. Consequently, the NRTL model is deemed the most suitable for simulation studies of the ethanol–water system, enabling more robust and reliable

Table 4
Binary interaction parameters obtained by regression of three thermodynamic models.

	NRTL	Wilson	UNIQUAC
a_{ij}	−6.277	−2.503	2.006
a_{ji}	6.968	−0.052	−2.492
b_{ij}	2150.945	352.978	−748.186
b_{ji}	−1762.433	−57.265	782.637
c_{ij}	0.300	0	0

Table 5
Deviations between calculated and experimental values of NRTL model.

T(exp)/°C	T(cal)/°C	ΔT/°C	x_1(exp)	x_1(cal)	Δx	y_1(exp)	y_1(cal)	Δy
100	100.01	0.01	0	0	0	0	0	0
96.15	96.24	0.09	0.015	0.014997	-3×10^{-6}	0.138	0.139422	0.001422
92.45	92.59	0.14	0.035	0.035001	1×10^{-6}	0.262	0.261423	−0.000577
86.65	86.56	−0.09	0.100	0.099991	-9×10^{-6}	0.435	0.437575	0.002575
83.52	83.52	0	0.182	0.182002	2×10^{-6}	0.524	0.520525	−0.003475
81.71	81.73	0.02	0.291	0.291011	1.1×10^{-5}	0.585	0.573757	−0.011243
80.70	80.69	−0.01	0.392	0.391996	-4×10^{-6}	0.609	0.608987	-1.3×10^{-5}
79.92	79.86	−0.06	0.502	0.501951	-4.9×10^{-5}	0.648	0.652132	0.004132
79.55	79.51	−0.04	0.542	0.541977	-2.3×10^{-5}	0.667	0.668156	0.001156
78.85	78.94	0.09	0.632	0.631916	-8.4×10^{-5}	0.712	0.710645	−0.001355
78.50	78.42	−0.08	0.748	0.747985	-1.5×10^{-5}	0.782	0.783283	0.001283
78.48	78.33	−0.15	0.794	0.793999	-1×10^{-6}	0.811	0.810557	−0.000443
78.25	78.2	−0.05	0.845	0.844996	-4×10^{-6}	0.854	0.854079	7.9×10^{-5}
78.18	78.17	−0.01	0.898	0.897991	-9×10^{-6}	0.899	0.899876	0.000876
78.23	78.21	−0.02	0.948	0.947995	-5×10^{-6}	0.945	0.945308	0.000308
78.30	78.31	0.01	1	1	0	1	1	0

Table 6
Deviations between calculated and experimental values of Wilson model.

T(exp)/°C	T(cal)/°C	ΔT/°C	x_1(exp)	x_1(cal)	Δx	y_1(exp)	y_1(cal)	Δy
100	100.03	0.03	0	0	0	0	0	0
96.15	96.02	−0.13	0.015	0.014991	-9×10^{-6}	0.138	0.145601	0.007601
92.45	92.50	0.05	0.035	0.034995	-5×10^{-6}	0.262	0.264065	0.002065
86.65	86.87	0.22	0.100	0.100011	1.1×10^{-5}	0.435	0.430842	−0.004158
83.52	83.89	0.37	0.182	0.182015	1.5×10^{-5}	0.524	0.516643	−0.007357
81.71	81.90	0.19	0.291	0.291009	9×10^{-6}	0.585	0.578906	−0.006094
80.70	80.70	0	0.392	0.391948	-5.2×10^{-5}	0.609	0.620298	0.011298
79.92	79.83	−0.09	0.502	0.501805	−0.000195	0.648	0.665902	0.017902
79.55	79.48	−0.07	0.542	0.541799	−0.000201	0.667	0.681803	0.014803
78.85	78.87	0.02	0.632	0.631901	-9.9×10^{-5}	0.712	0.722308	0.010308
78.50	78.34	−0.16	0.748	0.747915	-8.5×10^{-5}	0.782	0.789613	0.007613
78.48	78.22	−0.26	0.794	0.793945	-5.5×10^{-5}	0.811	0.814525	0.003525
78.25	78.12	−0.13	0.845	0.844972	-2.8×10^{-5}	0.854	0.855221	0.001221
78.18	78.08	−0.10	0.898	0.897991	-9×10^{-6}	0.899	0.898543	−0.000457
78.23	78.16	−0.07	0.948	0.948002	2×10^{-6}	0.945	0.94351	−0.00149
78.30	78.30	0	1	1	0	1	1	0

Table 7
Deviations between calculated and experimental values of UNIQUAC model.

T(exp)/°C	T(cal)/°C	ΔT/°C	x_1(exp)	x_1(cal)	Δx	y_1(exp)	y_1(cal)	Δy
100	100.02	0.02	0	0	0	0	0	0
96.15	96.14	−0.01	0.015	0.014985	-1.5×10^{-5}	0.138	0.142888	0.004888
92.45	92.54	0.09	0.035	0.034985	-1.5×10^{-5}	0.262	0.263982	0.001982
86.65	86.63	−0.02	0.100	0.099984	-1.6×10^{-5}	0.435	0.437633	0.002633
83.52	83.60	0.08	0.182	0.181992	-8×10^{-6}	0.524	0.522716	−0.001284
81.71	81.73	0.02	0.291	0.290993	-7×10^{-6}	0.585	0.579514	−0.005486
80.70	80.68	−0.02	0.392	0.391955	-4.5×10^{-5}	0.609	0.616455	0.007455
79.92	79.86	−0.06	0.502	0.501884	−0.000116	0.648	0.659763	0.011763
79.55	79.52	−0.03	0.542	0.543878	0.001878	0.667	0.675486	0.008486
78.85	78.96	0.11	0.632	0.631952	-4.8×10^{-5}	0.712	0.716882	0.004882
78.50	78.44	−0.06	0.748	0.747941	-5.9×10^{-5}	0.782	0.787205	0.005205
78.48	78.32	−0.16	0.794	0.793962	-3.8×10^{-5}	0.811	0.813431	0.002431
78.25	78.21	−0.04	0.845	0.844973	-2.7×10^{-5}	0.854	0.855707	0.001707
78.18	78.17	−0.01	0.898	0.897976	-2.4×10^{-5}	0.899	0.900342	0.001342
78.23	78.20	−0.03	0.948	0.947984	-1.6×10^{-5}	0.945	0.945202	0.000202
78.30	78.31	0.01	1	1	0	1	1	0

simulation results and providing a solid foundation for subsequent process optimization and simulation calculations.

2.3. Optimization methods and evaluation indicators

The total annual cost (TAC) is widely used for economic evaluation of chemical separation processes, so this study takes the minimum TAC as the optimization objective. The TAC calculation method reported in Ref. [27] has been widely recognized in the industry, and its expression is given by Eq. (14).

$$\mathrm{TAC} = \frac{\mathrm{TIC}}{3} + \mathrm{TOC} \tag{14}$$

where TIC denotes the total installed cost. This study primarily considers the core equipment of the distillation system, including

Table 8
Deviations between calculated and experimental values of three thermodynamic models.

Items	NRTL	Wilson	UNIQUAC
Maximum deviation, ΔT	−0.15	0.37	−0.16
Maximum deviation, Δx	-8.4×10^{-5}	−0.000201	0.001878
Maximum deviation, Δy	−0.011243	0.017902	0.011763
Average deviation, ΔT	−0.009375	−0.008125	−0.006875
Average deviation, Δx	-1.20×10^{-5}	-4.38×10^{-5}	9.03×10^{-5}
Average deviation, Δy	−0.000329688	0.00354875	0.002887875

the column shell, trays, and heat exchangers, while excluding the equipment costs of reflux drums, pumps, and valves. This simplification is based on the following considerations: compared with key equipment such as distillation columns and heat exchangers, the cost proportion of the former is extremely low, resulting in negligible impact on overall cost accounting. Furthermore, a 3-year payback period is set, which integrates industry standards and project revenue expectations. For the total operating cost (TOC), this study only accounts for three major expenses: heating steam, chilled water, and power consumption, as they account for a significant proportion of operating costs and have high data availability. Additionally, the annual operating hours are set at 8000 h, which is consistent with the typical annual operation cycle of chemical production units, ensuring the accuracy and rationality of production scale calculations.

Table 9 lists the detailed calculation formula for the TAC. When calculating the column equipment cost, the column height is first determined based on the number of trays (with a tray spacing set to 0.61 m), and the column diameter data are directly obtained from Aspen Plus software. After determining the column height and diameter, the main equipment cost of the column can be accurately calculated. For the heat exchanger cost calculation, the heat and cold load data provided by the simulation, combined with the heat transfer coefficients (0.852 $kW \cdot m^{-2} \cdot K^{-1}$ for the condenser and 0.568 $kW \cdot m^{-2} \cdot K^{-1}$ for the reboiler), are used to calculate the heat transfer area through temperature difference, thereby deriving the heat exchanger equipment cost. The unit prices of different grades of steam are as follows: low-pressure steam (160 °C) is 7.72 $USD \cdot GJ^{-1}$, medium-pressure steam (184 °C) is 8.22 $USD \cdot GJ^{-1}$, and high-pressure steam (260 °C) is 9.88 $USD \cdot GJ^{-1}$.

For the calculation of F_c in the equipment cost of the column shell, $F_c = F_m \times F_p$, where $F_m = 3.67$, and F_p can be obtained from Table 10. For the calculation of F_c in the equipment cost of the column plates, $F_c = F_s + F_t + F_m$, with $F_s = 1.0$, $F_t = 0$ (for sieve-plate columns), and $F_m = 1.7$. For the calculation of F_c in the cost of heat exchangers, $F_c = (F_d + F_p) \times F_m$, where $F_m = 3.75$, $F_d = 1.35$ (for reboilers), $F_d = 0.8$ (for fixed-tube-sheet heat exchangers), and F_p can be retrieved from Table 11. Q_R and Q_C represent the duties of the reboiler and condenser, respectively (in kW); λ_v is the latent heat of vaporization (in $kJ \cdot kg^{-1}$); C_S is the price of heating steam (in $USD \cdot kg^{-1}$). The Marshall and Swift cost inflation index, M&S, is taken as 1638.2.

Table 10
Values of F_p for calculating the cost of the column shell.

Pressure/MPa	≤0.34	0.68	1.36
F_p	1.00	1.05	1.15

Table 11
Values of F_p for calculating the cost of column plates.

Pressure/MPa	≤1.02	2.04	2.72	5.44
F_p	0.00	0.10	0.25	0.52

To systematically explore the environmental impact profiles of the integrated process, this study performed a comprehensive analysis of energy consumption in the separation unit. The energy consumption of the distillation process is predominantly derived from coal combustion for heating, a process that entails substantial emissions of greenhouse gases (GHGs), particularly CO_2. Consequently, this study designated CO_2 emissions as the pivotal metric for quantifying the environmental burden of the distillation process. The calculation methodology proposed by Li *et al.* [28] is outlined as follows:

$$M_{GAS} = A_{GAS} M_{Coal} + B_{GAS} W \tag{15}$$

$$M_{Coal} = Q_R \frac{N}{Q_{Standard}} \beta_{Coal,trans} \tag{16}$$

$$W = \frac{Q_{PUMP}}{\eta_{grid,trans}} \tag{17}$$

where, M_{GAS} (kg) represents the gas emission mass; M_{Coal} (kg) denotes the standard coal mass; A_{GAS} ($kg \cdot kW^{-1} \cdot h^{-1}$) and B_{GAS} ($kg \cdot kW^{-1} \cdot h^{-1}$) are the emission conversion coefficients for standard coal and electricity, respectively. The A_{GAS} and B_{GAS} values for different gases are listed in Table 12 [29]. N is the operating time, set to 8000 $h \cdot a^{-1}$ in this study; $\beta_{Coal,trans}$ is the isentropic efficiency (0.9); $Q_{Standard}$ is the standard coal calorific value

Table 9
Mathematical formulations for calculating the TAC.

Items		Calculation formula
Equipment cost/$USD \cdot a^{-1}$	Column height	$H = 1.2 \times 0.6096 \times (N_T - 2)$
	Equipment cost of the column shell	$C_1 = \left(\frac{M\&S}{280}\right) \times 937.636 \times ID^{1.066} \times H^{0.802} \times (2.18 + F_C)$
	Equipment cost of the plates	$C_2 = \left(\frac{M\&S}{280}\right) \times 97.243 \times ID^{1.55} \times H \times F_C$
	Heat transfer area of the condenser	$A_C = \frac{Q_C}{K_C \Delta T_C}$
	Cost of the condenser	$C_3 = \left(\frac{M\&S}{280}\right) \times 474.668 \times A_C^{0.65} \times (2.29 + F_C)$
	Heat transfer area of the reboiler	$A_R = \frac{Q_R}{K_R \Delta T_R}$
	Cost of the reboiler	$C_4 = \left(\frac{M\&S}{280}\right) \times 474.668 \times A_R^{0.65} \times (2.29 + F_C)$
Operating cost/$USD \cdot a^{-1}$	Steam	$C_S = \frac{Q_R}{\lambda_V} \times 3600 \times 8000$

Table 12
Emission conversion factors for CO_2.

Coefficient	CO_2
A_{GAS}/kg·kg^{-1}	2.493
B_{GAS}/kg·kW^{-1}·h^{-1}	0.997

(29307.6 kJ·kg^{-1}); $\eta_{grid,trans}$ represents the grid transmission efficiency (0.92).

3. High-Efficiency Distillation–Molecular Sieve Coupling Process

As shown in Fig. 2, the ethanol purification process proposed in this study integrates three-columns distillation with molecular sieve adsorption thermal coupling technology. The core process is as follows: The biomass feedstock solution derived from fermentation (ethanol mass concentration 3.5% to 5.5%) first enters the primary and secondary preheaters, where the waste heat from the bottom effluent of the crude distillation column and the waste liquids from the first distillation column and second distillation column is utilized as the heat source to raise the temperature of the feedstock to 57 °C and pressurize it to 0.1 MPa. It is then fed into the crude distillation column operating at an absolute pressure of 0.04–0.06 MPa with a top temperature maintained at 60–65 °C for preliminary separation. The vapor stream containing non-condensable gases such as CO_2 from the top of the crude distillation column enters a water scrubber, where impurities are removed by water washing before returning to the column top, effectively reducing ethanol loss. Meanwhile, the liquid stream withdrawn from the column top is transported to the second distillation column (absolute pressure 0.40–0.60 MPa, top temperature 120–125 °C) for deep purification, while the intermediate component stream withdrawn from the side line enters the first distillation column (absolute pressure 0.10–0.30 MPa, top temperature 100–110 °C) for further refining. In the first distillation column, the ethanol vapor from the column top (reflux ratio 1.0–4.0) serves as the heat source for the reboiler at the bottom of the crude distillation column. After heat exchange with the column bottom medium, part of the ethanol vapor condenses and returns to the column as reflux, while the remaining vapor is combined with the vapor from the top of the second distillation column (reflux ratio 4.5–8.0). The vapor from the top of the second distillation column simultaneously supplies heat to the reboiler at the bottom of the first distillation column. After gas–liquid separation, the bottom liquid of the two distillation columns is processed such that the gas phase returns to the column to maintain distillation equilibrium, and the liquid waste serves as a heat source for the feed preheater, maximizing waste heat recovery.

The streams withdrawn from the tops of the first and second distillation columns undergo multi-stage heat exchange, with part returning as reflux and the rest combined into a molecular sieve adsorption bed (3A molecular sieve, operated at 170 °C under atmospheric pressure). Residual moisture is deeply removed *via* selective adsorption, yielding fuel ethanol products with a purity of 99.95%, while the adsorbed waste liquid is discharged from the system. The process employs thermal coupling technologies, including three-columns differential pressure design (cooperation of low, medium, and high pressures), top vapor-bottom medium heat exchange, and waste liquid heat recovery, to reduce external steam demand and achieve a 50% energy consumption reduction compared to conventional processes. Meanwhile, the process shortens the production route, improves ethanol yield and product quality, and has application value for the industrial production of high-purity ethanol products such as fuel ethanol and medical ethanol.

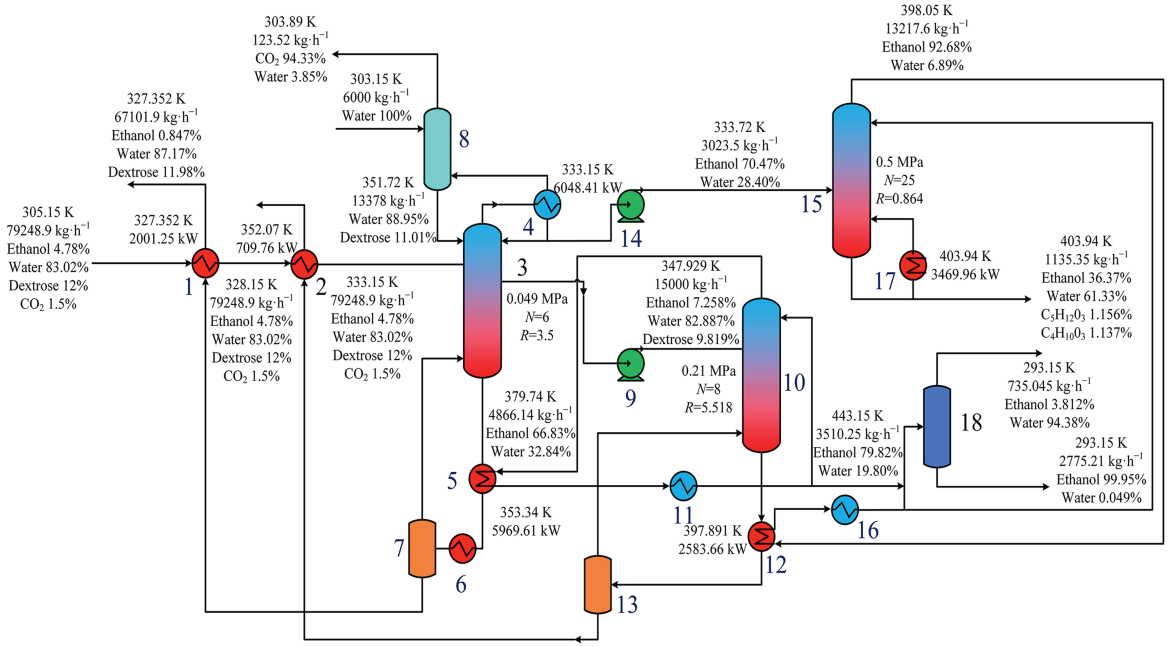

Fig. 2. Schematic of high-efficiency distillation-molecular sieve coupling process: (1) primary preheater 1, (2) primary preheater 2, (3) crude distillation column, (4) overhead condenser of crude distillation column, (5) bottom reboiler of crude distillation column, (6) auxiliary reboiler, (7) bottom gas–liquid separator of crude distillation column, (8) water scrubber, (9) feed pump of first distillation column, (10) first distillation column, (11) auxiliary condenser 1, (12) bottom reboiler of first distillation column, (13) bottom gas–liquid separator of first distillation column, (14) feed pump of second distillation column, (15) second distillation column, (16) auxiliary condenser 2, (17) bottom reboiler of second distillation column, (18) molecular sieve adsorption bed.

4. Aspen Simulation Optimization of High-Efficiency Distillation–Molecular Sieve Coupling Process

The ethanol refining process developed in this study integrates three-columns distillation with molecular sieve adsorption thermal coupling technology. After preheating with bottom waste heat, the feedstock solution first enters the crude distillation column for preliminary separation. The vapor stream from the top of the crude distillation column is returned to the column after impurity removal, while the side-line components and top liquid stream enter the first and second distillation columns for deep purification, respectively. The three-columns differential pressure design constructs an efficient thermal integration network: the vapors from the medium-pressure and high-pressure columns serve as mutual heat sources. After gas–liquid separation, the bottom liquid of the columns is processed such that the gas phase returns to maintain distillation equilibrium, and the liquid phase preheats the feedstock as a heat source, achieving cascade utilization of waste heat. Part of the overhead stream from the distillation columns is recycled after heat exchange, and the remaining part is dehydrated *via* selective adsorption by molecular sieves to obtain high-purity ethanol products. The process reduces energy consumption and shortens the process flow through multi-stage thermal coupling and deep process integration, while improving ethanol production efficiency and product quality.

To ensure separation efficiency, strict standards are set for the mass fractions of product ethanol and water: the ethanol mass fraction is not lower than 99.6%, and the water mass fraction is not lower than 99.8%. Aspen Plus process simulation software is used for scheme design and optimization, and the simulation flow is shown in Fig. 3. The *RadFrac* rigorous calculation model is adopted for the distillation column unit, the Heater module is used for heat exchangers, and the NRTL activity coefficient model is selected as the physical property method. Key separation indicators are set in the simulation: the ethanol mass fraction at the top of the crude distillation column is $\geq$ 62.5%, that of the first distillation column is $\geq$ 50.0%, that of the second distillation column is $\geq$ 92.0%, and the ethanol mass fraction of the molecular sieve separation product is $\geq$ 99.4%. In the distillation-molecular sieve coupling separation, special attention should be paid to the homogeneous azeotrope characteristics of the ethanol–water system—the traditional DSTWU simple distillation module is difficult to effectively estimate key process parameters such as the number of theoretical trays and minimum reflux ratio. Therefore, this study uses Aspen Plus to perform sensitivity analysis on operating parameters, determines the optimal process parameter combination through precise optimization, provides data support for the optimal design and efficient operation of heat pump distillation, and improves the economic efficiency and engineering feasibility of the production process.

In the initial setting of operating parameters for the distillation process, the reflux mass ratio is set to 3.0, and the feed location is selected as the theoretical tray number minus 3. This setting aims to ensure that the separation operation runs in the optimal energy efficiency interval, while ensuring that the product purity meets technical specifications, achieving a balance between economic benefits and separation efficiency.

Analysis of the data shown in Fig. 3 indicates that when the number of theoretical trays is less than 6, the overhead ethanol concentration of the crude distillation column increases significantly and rapidly with the increase in the number of theoretical trays, while the steam consumption decreases sharply. When the number of theoretical trays exceeds 6, further increasing the number of theoretical trays leads to a gradual flattening of changes in both the overhead ethanol concentration and steam consumption. Considering factors such as separation efficiency and equipment cost, the optimal number of theoretical trays for the pressurized column is determined to be 6. At this point, the mass concentration of ethanol at the column top can reach 70.61%, and the steam consumption is relatively low, achieving a balance between separation efficiency and cost control.

As shown in Fig. 4, when the feed location in the crude distillation column is moved toward the column bottom, the overhead ethanol mass concentration exhibits a trend of first gradually increasing and then sharply decreasing. This is because when the feed location is close to the column top, the number of theoretical trays in the rectifying section is insufficient to achieve efficient separation; conversely, when the feed location is close to the column bottom, the number of theoretical trays in the stripping section is insufficient, similarly hindering the improvement of separation efficiency. Furthermore, lowering the feed location increases the reboiler load, thereby affecting the separation process. When the feed location is between the 2nd and 5th theoretical trays, the overhead ethanol mass concentration meets the separation requirements. Considering both separation efficiency and energy consumption, the optimal feed location for the pressurized

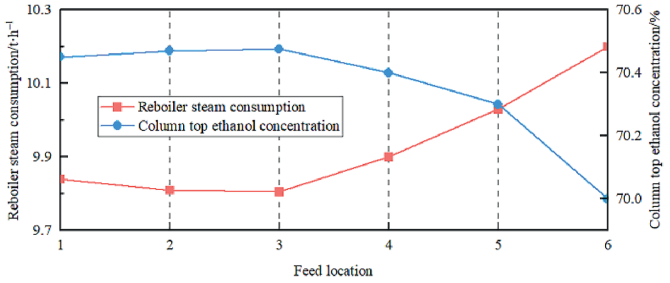

Fig. 4. Effects of feed location in crude distillation column on reboiler heat duty and column top ethanol mass concentration.

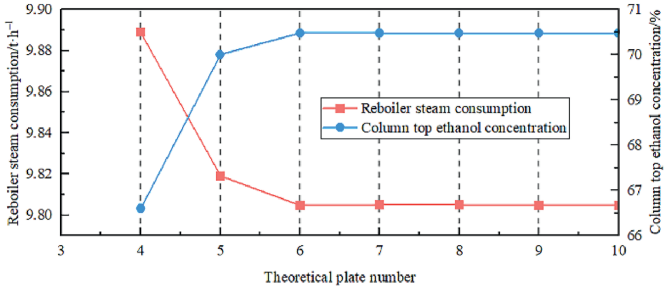

Fig. 3. Effects of theoretical plate number of crude distillation column on reboiler heat duty and column top ethanol mass concentration.

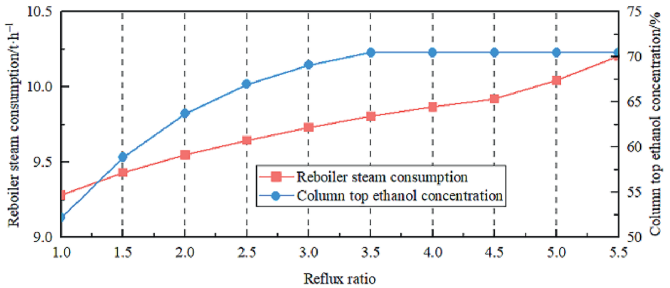

Fig. 5. Effects of reflux ratio in crude distillation column on reboiler heat duty and column top ethanol mass concentration.

column is determined to be the 3rd theoretical tray. At this location, the ethanol content at the column top reaches a peak, with a mass concentration of 70.46%, effectively balancing separation performance and energy consumption.

With the number of theoretical trays set to 6 and the feed location fixed at the 3rd theoretical tray, other operating parameters were kept constant while adjusting the key variable of reflux ratio to investigate its effect on product quality and steam consumption. The simulation results are shown in Fig. 5.

Analysis of the data in Fig. 5 indicates that moderately increasing the reflux ratio can significantly improve product quality. However, increasing the reflux ratio leads to an increase in gas–liquid phase loads within the column, thereby raising the reboiler load. Simulation results show that the overhead ethanol content in the crude distillation column initially increases significantly and then levels off with increasing reflux ratio. Considering both product quality and reboiler energy consumption, the reflux ratio is set to 3.5 when the overhead ethanol content reaches approximately 71.23%. At this point, the reboiler load is relatively low, enabling the system to achieve an effective balance between product quality and energy consumption under this operating condition.

In this study, the side draw of the crude distillation column is the ethanol product, and the side draw location has a significant impact on product quality and energy consumption. Thus, with the number of theoretical trays set to 6, the feed location fixed at the 3rd theoretical tray, and the reflux ratio set to 3.5, the influence of the side draw location was simulated, and the results are shown in Fig. 6. The 3rd theoretical tray is the feed tray, with the rectifying section above it mainly containing light components in the feed and ethanol–water azeotropes, and the stripping section below it primarily used for heavy component concentration. When the side draw location is less than 3, the ethanol content in the side draw material is low and shows no obvious change; when the side draw location is greater than 3, the ethanol content first increases rapidly with the downward movement of the side draw location and then levels off near the column bottom. A comprehensive analysis determines that the optimal side draw location is the 4th theoretical tray.

The separation efficiency of the first and second distillation columns is affected by key variables such as the number of theoretical trays, feed inlet location, reflux ratio, and circulation flow rate. Since the separation performance of the two columns directly affects the product quality of the side draw from the crude distillation column and the purity of the overhead product, the comprehensive influence of these variables on the core operating indicators of the two columns must be evaluated simultaneously when optimizing the operating parameters of the distillation columns. The analysis framework for the crude distillation column can be used for sensitivity analysis, and Figs. 7–12 systematically show the influence laws of the number of theoretical trays, feed location, and reflux ratio of the two distillation columns on the main operating parameters. Specifically, fine-tuning of key parameters will affect the separation efficiency and thermal energy consumption of the distillation process to varying degrees. In practical operation, a balance between separation efficiency and energy consumption control must be achieved through collaborative optimization of multiple variables (see Figs. 13–15).

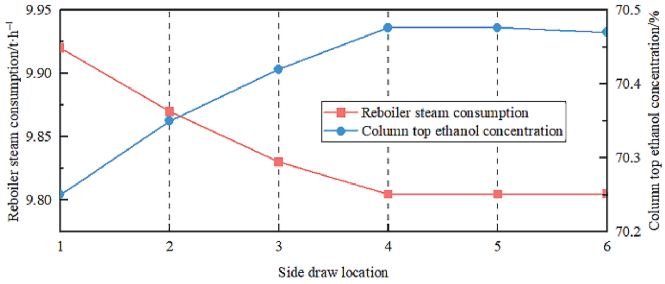

Fig. 6. Effects of side draw location in crude distillation column on reboiler heat duty and column top ethanol mass concentration.

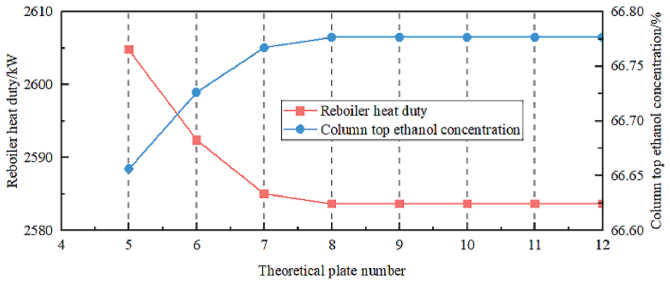

Fig. 7. Effects of theoretical plate number of first distillation column on reboiler heat duty and column top ethanol mass concentration.

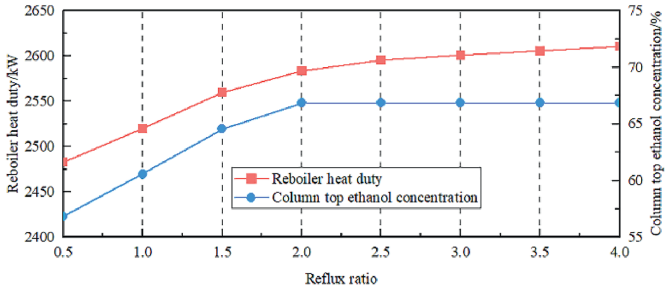

Fig. 8. Effects of reflux ratio of first distillation column on reboiler heat duty and column top ethanol mass concentration.

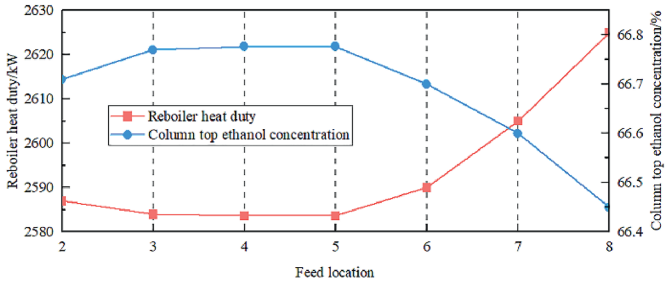

Fig. 9. Effects of feed location in first distillation column on reboiler heat duty and column top ethanol mass concentration.

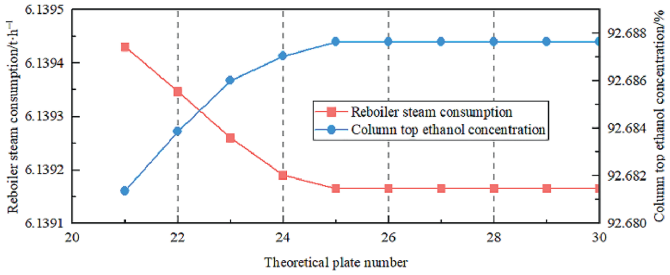

Fig. 10. Effects of theoretical plate number of second distillation column on reboiler heat duty and column top ethanol mass concentration.

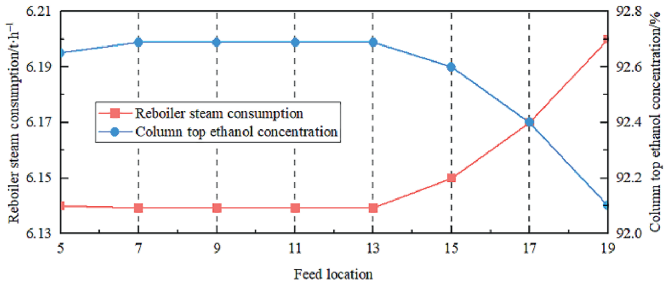

Fig. 11. Effects of feed location in second distillation column on reboiler heat duty and column top ethanol mass concentration.

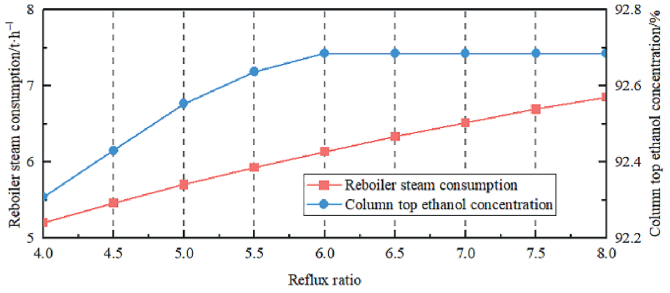

Fig. 12. Effects of reflux ratio in second distillation column on reboiler heat duty and column top ethanol mass concentration.

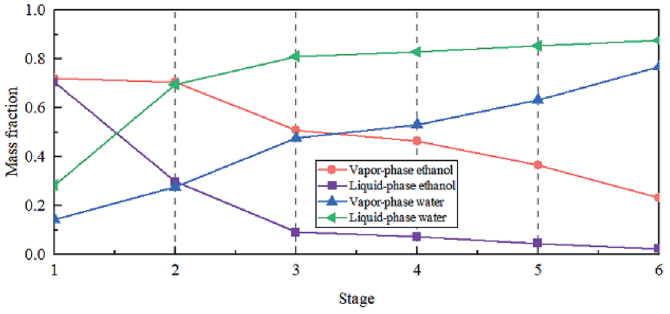

Fig. 13. Gas–liquid distributions on plates of crude distillation column.

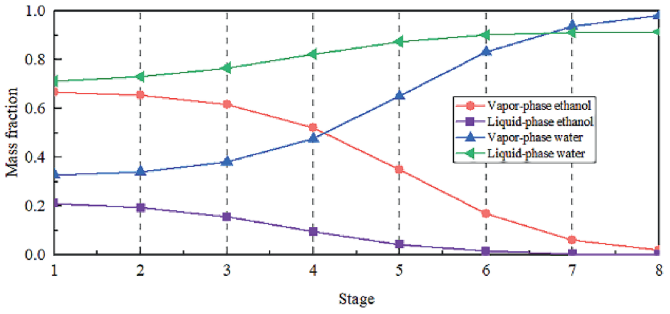

Fig. 14. Gas–liquid distributions on plates of first distillation column.

Based on the comprehensive consideration of the above sensitivity analysis results, Table 13 summarizes the optimal operating parameters of each column obtained from the simulation of the ethanol–water distillation-molecular sieve coupling system.

In the high-efficiency distillation–molecular sieve coupling process, the differences in gas–liquid distribution curve trends of

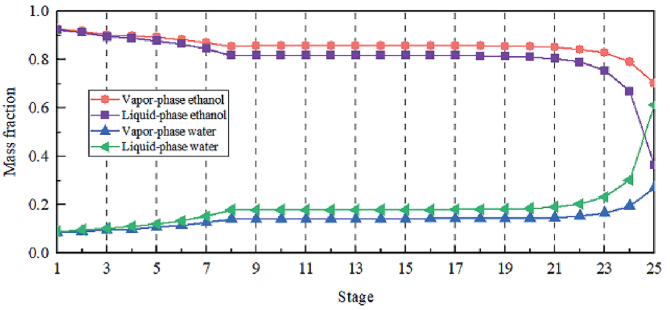

Fig. 15. Gas–liquid distributions on plates of second distillation column.

each column are primarily influenced by the combined effects of component volatility, tray efficiency, and molecular sieve action. In the crude distillation column, the difference in relative volatility between ethanol and water leads to the gradual enrichment of ethanol concentration in the gas phase with increasing tray number, while liquid water accumulates in the lower trays due to its high boiling point property. In the first distillation column, adjusting the reflux ratio enhances the separation efficiency, causing the ethanol concentration in both gas and liquid phases to reach equilibrium near the middle trays, whereas water components significantly decrease in subsequent trays due to the adsorption effect of molecular sieves. In the second distillation column, the deep dehydration effect of molecular sieves further improves the purity of ethanol in the gas phase, with liquid water almost completely removed and the curve flattening out. These trends reflect the improvement in component separation efficiency during the stepwise purification process and the directional regulation of gas–liquid equilibrium by molecular sieves.

5. Comparative Economic Analysis of High-Efficiency Distillation–Molecular Sieve Coupling Process and Conventional Three-columns Distillation

As shown in Fig. 16, this study conducts a systematic comparative analysis of the conventional three-columns distillation process and the high-efficiency distillation–molecular sieve coupling process, based on the ethanol–water three-columns distillation process widely applied in industrial fields in recent years [30–33]. To ensure the scientific validity and rigor of the comparison, the high-efficiency distillation–molecular sieve coupling process maintains consistent feed composition and flow parameters with the conventional process, with the only variable being the process type. As presented in Table 14, by comprehensively comparing the differences between the two processes in key indicators such as CO_2 emission costs and overall costs, the improvement effect of the high-efficiency process is accurately quantified, and its superiority and feasibility are fully verified. This comparative approach not only ensures the reliability of research findings but also provides robust theoretical support and practical evidence for the industrial implementation of the high-efficiency process.

The high-efficiency distillation-molecular sieve coupling process developed in this study employs 3A molecular sieves with a unit price of 554 USD·t^{-1}, where the material cost of molecular sieves accounts for approximately 2.6% of the adsorption column equipment cost. Compared with the conventional three-columns process, this process reduces CO_2 emission costs by 27.56%, with a TAC of 5.123 × 10^6 USD·a^{-1}—representing a 15.58% reduction from the conventional three-columns distillation process.

In terms of mechanism application and Aspen simulation integration, this study borrows the differential element balance concept

Table 13
Optimal process parameters of each column in high-efficiency distillation-molecular sieve coupling process.

Column	Theoretical plates	Feed location	Reflux ratio	Side-draw location
Crude distillation column	6	3	3.50	4
First distillation column	8	5	5.51	–
Second distillation column	25	13	0.86	–

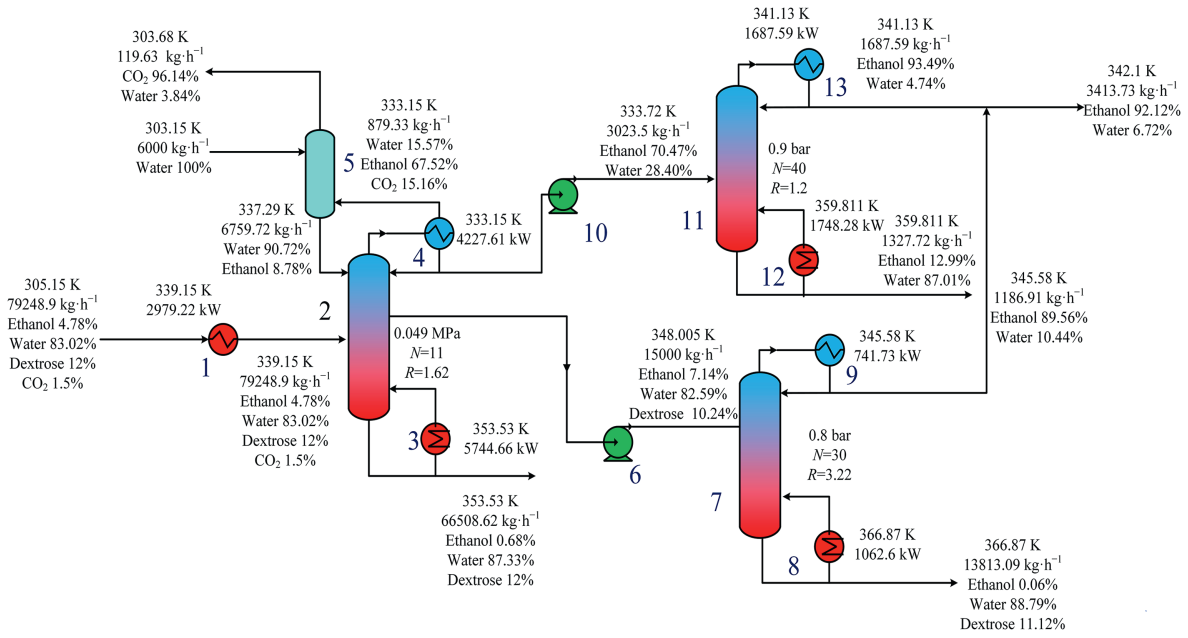

Fig. 16. Process flow of conventional three-columns distillation: (1) primary preheater, (2) crude distillation column, (3) reboiler of crude distillation column, (4) condenser of crude distillation column, (5) water washing column, (6) feed pump for first distillation column, (7) first distillation column, (8) reboiler of first distillation column, (9) condenser of first distillation column, (10) feed pump for second distillation column, (11) second distillation column, (12) reboiler of second distillation column, (13) condenser of second distillation column.

Table 14
Economic comparison between high-efficiency distillation–molecular sieve coupling process and conventional three-columns distillation.

Process Type	Feed flow rate/kg·h^{-1}	Ethanol mass fraction/%	Distillation column cost		CO_2 emission cost/USD·a^{-1}	TAC/USD·a^{-1}
			TCC/USD·a^{-1}	TOC/USD·a^{-1}		
High-efficiency distillation–molecular sieve coupling process	7.925×10^4	4.78	7.347×10^6	1.419×10^6	1.628×10^5	5.123×10^6
Conventional three-columns distillation process	7.925×10^4	4.78	8.156×10^6	3.126×10^6	2.247×10^5	6.069×10^6

from membrane separation, treating the molecular sieve adsorption process as a dynamic mass transfer unit. The RYield model is used in the simulation to mimic the selective adsorption of water molecules by molecular sieves, with an adsorption capacity set at 0.3 kg water per kg molecular sieve. The bulk density $\rho_b = 729\ kg \cdot m^{-3}$ and gas mass velocity $G = 0.863\ kg \cdot m^{-2} \cdot s^{-1}$ are coupled into the distillation column module, leading to the optimized design of the adsorption column with a height of 5.397 m and a diameter of 1.199 m. By segmenting the adsorption–desorption cycle period, a quantitative description of the "size sieving effect" and "polar adsorption" mechanisms is achieved, ultimately increasing the ethanol purity to 99.6%.

6. Conclusions

This study aimed to address the high energy consumption and significant costs associated with the conventional three-columns distillation process in cellulosic ethanol separation. An innovative high-efficiency distillation–molecular sieve coupling process was developed, and process parameters were systematically optimized using the Aspen Plus simulation platform. The thermodynamic characteristics and economic competitiveness of different processes were thoroughly analyzed. The core of this process lies in constructing a thermal coupling network and cascading utilization of waste heat. Through the synergistic effect of multiple technologies, it overcomes traditional separation bottlenecks. The size sieving and polar adsorption properties of 3A molecular sieves are harnessed to achieve deep dehydration. Simulation results indicate that, compared with the conventional three-columns process, the new process reduces CO_2 emission costs by 27.56% and decreases the TAC to 5.123×10^6 USD·a^{-1}, representing a 15.58% reduction. However, the regeneration energy consumption of molecular sieves limits its economic advantages to some extent. Through process intensification and technology integration, this study provides a viable solution for the green manufacturing of cellulosic ethanol. Future research could further explore the tandem process of molecular sieves and

membrane separation to achieve synergistic enhancement of "selective adsorption–pervaporation," thereby further reducing separation energy consumption. In summary, the high-efficiency distillation–molecular sieve coupling process proposed in this study offers theoretical and technical support for solving high-energy-consumption problems in the biomass energy field and holds significant implications for promoting the industrial development of renewable energy.

CRediT Authorship Contribution Statement

Xuefeng Feng: Writing – original draft, Software, Methodology, Investigation, Formal analysis, Conceptualization. Shuaishuai Lu: Writing – original draft, Validation, Data curation. Xuan Du: Visualization, Software, Investigation. Shaolan Zhuang: Writing – review & editing, Supervision, Resources. Zhongqi Ren: Writing – review & editing, Supervision. Zhongwei Ding: Funding acquisition, Supervision. Qunsheng Li: Writing – review & editing, Supervision, Resources, Funding acquisition, Conceptualization. Weiying Feng: Writing – review & editing, Supervision, Resources, Funding acquisition, Conceptualization. Hongkang Zhao: Writing – review & editing, Supervision, Resources, Funding acquisition, Conceptualization.

Declaration of Competing Interest

The authors declare that they have no known competing financial interests or personal relationships that could have appeared to influence the work reported in this paper.

Acknowledgements

We are thankful for financial support from the National Key Research and Development Program of China (2022YFC2106300) and the National Natural Science Foundation of China (42177400).

References

[1] M.A.S.S. Ravagnani, M.H.M. Reis, R.M. Filho, M.R. Wolf-Maciel, Anhydrous ethanol production by extractive distillation: a solvent case study, *Process Saf. Environ. Prot.* 88 (1) (2010) 67–73.
[2] V. Gomis, R. Pedraza, M.D. Saquete, A. Font, J. García-Cano, Ethanol dehydration *via* azeotropic distillation with gasoline fraction mixtures as entrainers: a pilot-scale study with industrially produced bioethanol and naphta, *Fuel Process. Technol.* 140 (2015) 198–204.
[3] S.K. Abdul Mudalip, A. Ripin, R. Mohd Yunus, S.Z. Sulaiman, R. Che Man, Effects of ultrasonic waves on vapor–liquid equilibrium of cyclohexane/benzene, *Int. J. Adv. Sci. Eng. Inf. Technol.* 1 (1) (2011) 72.
[4] K.Y. Hsu, Y.C. Hsiao, I.L. Chien, Design and control of dimethyl carbonate–methanol separation *via* extractive distillation in the dimethyl carbonate reactive-distillation process, *Ind. Eng. Chem. Res.* 49 (2) (2010) 735–749.
[5] J. Holtbruegge, M. Wierschem, S. Steinruecken, D. Voss, L. Parhomenko, P. Lutze, Experimental investigation, modeling and scale-up of hydrophilic vapor permeation membranes: separation of azeotropic dimethyl carbonate/methanol mixtures, *Sep. Purif. Technol.* 118 (2013) 862–878.
[6] I.D. Gil, A.M. Uyazán, J.L. Aguilar, G. Rodríguez, L.A. Caicedo, Separation of ethanol and water by extractive distillation with salt and solvent as entrainer: process simulation, *Braz. J. Chem. Eng.* 25 (1) (2008) 207–215.
[7] S. Majidi Salehi, G. Di Profio, E. Fontananova, F.P. Nicoletta, E. Curcio, G. De Filpo, Membrane distillation by novel hydrogel composite membranes, *J. Membr. Sci.* 504 (2016) 220–229.
[8] Z.Y. Zhu, L.L. Wang, Y.X. Ma, W.L. Wang, Y.L. Wang, Separating an azeotropic mixture of toluene and ethanol *via* heat integration pressure swing distillation, *Comput. Chem. Eng.* 76 (2015) 137–149.
[9] M. Kondo, H. Kita, Permeation mechanism through zeolite NaA and T-type membranes for practical dehydration of organic solvents, *J. Membr. Sci.* 361 (1–2) (2010) 223–231.
[10] G.X. Li, S.L. Liu, G.Q. Yu, C.N. Dai, Z.G. Lei, Extractive distillation using ionic liquids-based mixed solvents combined with dividing wall column, *Sep. Purif. Technol.* 269 (2021) 118713.
[11] T. Mahdi, A. Ahmad, M.M. Nasef, A. Ripin, State-of-the-art technologies for separation of azeotropic mixtures, *Sep. Purif. Rev.* 44 (4) (2015) 308–330.
[12] A.C. Dimian, C.S. Bildea, A.A. Kiss, Integrated Design and Simulation of Chemical Processes, Elsevier, Amsterdam, 2014.
[13] K. Koch, A. Górak, Pervaporation of binary and ternary mixtures of acetone, isopropyl alcohol and water using polymeric membranes: experimental characterisation and modelling, *Chem. Eng. Sci.* 115 (2014) 95–114.
[14] P.D.A. Bastos, F.S. Oliveira, L.P.N. Rebelo, A.B. Pereiro, I.M. Marrucho, Separation of azeotropic mixtures using high ionicity ionic liquids based on 1-ethyl-3-methylimidazolium thiocyanate, *Fluid Phase Equilib.* 389 (2015) 48–54.
[15] X.Q. You, I. Rodriguez-Donis, V. Gerbaud, Low pressure design for reducing energy cost of extractive distillation for separating diisopropyl ether and isopropyl alcohol, *Chem. Eng. Res. Des.* 109 (2016) 540–552.
[16] P. Lutze, A. Gorak, Reactive and membrane-assisted distillation: recent developments and perspective, *Chem. Eng. Res. Des.* 91 (10) (2013) 1978–1997.
[17] N.R. Rodríguez, A.S.B. González, P.M.A. Tijssen, M.C. Kroon, Low transition temperature mixtures (LTTMs) as novel entrainers in extractive distillation, *Fluid Phase Equilib.* 385 (2015) 72–78.
[18] C.M. Gong, H. Gao, P. Wu, J.S. Sun, J. Li, Hybrid distillation-biomass adsorption process for isopropanol–water azeotrope separation, *Asia Pac. J. Chem. Eng.* 8 (1) (2013) 77–84.
[19] W.S. Li, L. Shi, B.R. Yu, M. Xia, J.W. Luo, H.C. Shi, C.J. Xu, New pressure-swing distillation for separating pressure-insensitive maximum boiling azeotrope *via* introducing a heavy entrainer: design and control, *Ind. Eng. Chem. Res.* 52 (23) (2013) 7836–7853.
[20] Y. Huang, R.W. Baker, L.M. Vane, Low-energy distillation-membrane separation process, *Ind. Eng. Chem. Res.* 49 (8) (2010) 3760–3768.
[21] P.K. Sharma, P.C. Wankat, Distillation–adsorption hybrid processes to separate binary liquid mixtures with homogeneous azeotrope, *Sep. Sci. Technol.* 48 (1) (2013) 1–14.
[22] J.A. Ritter, F. Wu, A.D. Ebner, New approach for modeling hybrid pressure swing adsorption–distillation processes, *Ind. Eng. Chem. Res.* 51 (27) (2012) 9343–9355.
[23] K.S. Wang, C.C. Liao, R.Q. Chu, T.W. Chung, Equilibrium isotherms of water and ethanol vapors on starch sorbents and zeolite 3A, *J. Chem. Eng. Data* 55 (9) (2010) 3334–3337.
[24] A. Chaibi, Y. Boucheffa, N. Bendjaballah-Lalaoui, TGA investigation of water and ethanol adsorption over LTA zeolites, *Micropor. Mesopor. Mater.* 324 (2021) 111285.
[25] E. Gabruś, J. Nastaj, P. Tabero, T. Aleksandrzak, Experimental studies on 3A and 4A zeolite molecular sieves regeneration in TSA process: aliphatic alcohols dewatering–water desorption, *Chem. Eng. J.* 259 (2015) 232–242.
[26] J.M. Prausnitz, C.A. Eckert, R.V. Orye, J.P. OConnell, Computer Calculations for Multicomponent vapor–liquid Equilibria, Prentice-Hall, Englewood Cliffs, 1967.
[27] Q.S. Li, N. Hu, S.P. Zhang, Q.P. Wu, J. Qi, Energy-saving heat integrated extraction-azeotropic distillation for separating isobutanol–ethanol–water, *Sep. Purif. Technol.* 255 (2021) 117695.
[28] X.Q. Li, Y.F. Zhang, L. Fang, Z.D. Jin, Y. Zhang, X.H. Yu, X.L. Ma, N. Deng, Z.X. Wu, Energy, exergy, economic, and environmental analysis of an integrated system of high-temperature heat pump and gas separation unit, *Energy Convers. Manag.* 198 (2019) 111911.
[29] B.M. Dai, H.F. Qi, S.C. Liu, Z.F. Zhong, H.L. Li, M.J. Song, M.Y. Ma, Z.L. Sun, Environmental and economical analyses of transcritical CO_2 heat pump combined with direct dedicated mechanical subcooling (DMS) for space heating in China, *Energy Convers. Manag.* 198 (2019) 111317.
[30] Y.Q. Lan, N. Yan, W.H. Wang, Application of PDMS pervaporation membranes filled with tree bark biochar for ethanol/water separation, *RSC Adv.* 6 (53) (2016) 47637–47645.
[31] S. Hernández, J. Gabriel Segovia-Hernández, V. Rico-Ramírez, Thermodynamically equivalent distillation schemes to the Petlyuk column for ternary mixtures, *Energy* 31 (12) (2006) 2176–2183.
[32] M.B. Yang, X. Feng, G.L. Liu, Heat integration of heat pump assisted distillation into the overall process, *Appl. Energy* 162 (2016) 1–10.
[33] A.K. Jana, Advances in heat pump assisted distillation column: a review, *Energy Convers. Manag.* 77 (2014) 287–297.